AGU PUBLICATIONS

Water Resources Research

RESEARCH ARTICLE

10.1002/2016WR020260

Impact of spatially correlated pore-scale heterogeneity on drying porous media

Oshri Borgman[1], Paolo Fantinel[2], Wieland Lühder[2], Lucas Goehring[2,3], and Ran Holtzman[1]

[1]Department of Soil and Water Sciences, Hebrew University of Jerusalem, Rehovot, Israel, [2]Max Planck Institute for Dynamics and Self-Organization, Göttingen, Germany, [3]School of Science and Technology, Nottingham Trent University, Nottingham, UK

Key Points:
- We combine a pore-scale model of isothermal drying of porous media with state-of-the-art microfluidic experiments of the same pore geometry
- Increasing spatial correlation of particle size promotes preferential drying of large pores
- Preferential drying prolongs liquid connectivity and surface wetness, delaying the rate drop characterizing transition between drying stages

Supporting Information:
- Supporting Information S1
- Movie S1
- Movie S2

Correspondence to:
R. Holtzman,
holtzman.ran@mail.huji.ac.il

Citation:
Borgman, O., P. Fantinel, W. Lühder, L. Goehring, and R. Holtzman (2017), Impact of spatially correlated pore-scale heterogeneity on drying porous media, *Water Resour. Res.*, *53*, doi:10.1002/2016WR020260.

Received 15 DEC 2016
Accepted 13 JUN 2017
Accepted article online 16 JUN 2017

Abstract We study the effect of spatially-correlated heterogeneity on isothermal drying of porous media. We combine a minimal pore-scale model with microfluidic experiments with the same pore geometry. Our simulated drying behavior compares favorably with experiments, considering the large sensitivity of the emergent behavior to the uncertainty associated with even small manufacturing errors. We show that increasing the correlation length in particle sizes promotes preferential drying of clusters of large pores, prolonging liquid connectivity and surface wetness and thus higher drying rates for longer periods. Our findings improve our quantitative understanding of how pore-scale heterogeneity impacts drying, which plays a role in a wide range of processes ranging from fuel cells to curing of paints and cements to global budgets of energy, water and solutes in soils.

Plain Language Summary Drying of porous media such as soils, cement, food or fuel cells is an important process in many natural and industrial systems. Drying in soils is of particular environmental importance, as it controls the transfer of water, energy and solutes between the subsurface and the atmosphere. We study the effect of spatial correlation in particle sizes on drying rate and extent, by combining pore-scale modeling with state-of-the-art microfluidic experiments of the same pore geometry. Our simulations compare favorably with experiments, considering the large sensitivity of the emergent behavior to the uncertainty associated with manufacturing errors. We show that increasing the correlation length in particle sizes–the distance in which the probability to encounter particles of similar sizes is high–promotes preferential invasion of clusters of large pores, prolonging liquid connectivity and surface wetness and thus higher drying rates for longer periods. Our findings improve our understanding of how pore-scale heterogeneity, inevitable in most porous materials, affects their drying.

1. Introduction

Drying of porous media plays a crucial role in many natural and industrial systems, from soils, to curing of cement, paints and food [*Prat*, 2011; *Goehring et al*., 2015]. Drying in soils is of particular environmental importance, as it controls the transfer of water and energy between the subsurface and the atmosphere and affects solute distribution in the root zone [*Or et al*., 2013]. The rate and extent of fluid transport in general, and drying in particular, intimately depend on the heterogenous distribution of grain and pore sizes and their connectivity, among other factors [*Bultreys et al*., 2016; *Holtzman*, 2016]. Pore-size heterogeneity, either random (disordered) or spatially-correlated in the form of patches or layers of finer or coarser particles, is an inherent property of natural porous media such as soils or sediments [*Knackstedt et al*., 2001], resulting from deposition and diagenetic processes. Even in engineered systems such as micromodels, heterogeneity is inevitable due to manufacturing errors.

In this paper, we investigate how spatial correlation in particle sizes affects isothermal drying of porous media, where evaporation is driven by vapor concentration differences between the medium and the outside atmosphere. Evaporation reduces the liquid pressure, allowing air to invade into the pores once the capillary entry thresholds are exceeded, forming an interface separating liquid- and air-filled pores [*Lehmann et al*., 2008; *Shokri et al*., 2010]. The drying process is typically divided into two main stages. During stage 1 (also called the "constant rate period"), evaporation occurs mostly from wet patches at the

medium's surface, while liquid is supplied by continuous pathways from the medium's interior. Stage 1 is characterized by a drying rate which remains fairly constant despite the decline in surface wetness; this is attributed to vapor transport in an air boundary layer that develops outside the medium [*Yiotis et al*., 2007; *Lehmann et al*., 2008; *Shokri et al*., 2010; *Shahraeeni et al*., 2012]. Stage 2 (or the "falling-rate period") is marked by a disruption of the liquid pathways to the surface, forcing the surface pores to dry out and the evaporation to occur further away from the surface. Consequently, the rate, which becomes limited by vapor diffusion within the porous medium, drops continuously [*Lehmann et al*., 2008; *Shokri et al*., 2010; *Goehring et al*., 2015]. Liquid connectivity to the surface can be further enhanced by liquid films, in systems such as throat networks with channels of noncircular cross section or with rough walls, and granular media [*Laurindo and Prat*, 1998; *Eijkel et al*., 2005; *Yiotis et al*., 2012, 2015].

Previous studies have shown that when a sharp contrast in pore sizes exists (in the form of a coarser and a finer region), the coarser region dries up completely before finer pores starts to dry. This has been demonstrated experimentally for a variety of media of different length scales, including sands [*Lehmann and Or*, 2009; *Nachshon et al*., 2011; *Assouline et al*., 2014], micromodels [*Pillai et al*., 2009] and colloidal drops [*Xu et al*., 2008]. Theoretically it has been shown that increasing the width of the pore-size distribution prolongs stage 1 by maintaining liquid connectivity for longer periods [*Metzger and Tsotsas*, 2005; *Lehmann et al*., 2008]. We note that this observation is true only when gravitational or viscous forces are sufficiently large, e.g., in a sufficiently deep sample. Nonetheless, a systematic study of how the correlation length of grain or particle sizes (defined as the characteristic length scale over which particles of similar sizes are expected) affects drying is lacking.

For the more general problem of immiscible fluid-fluid displacement, it has been shown that increasing correlation length decreases the residual saturation of the wetting phase at breakthrough [*Ioannidis et al*., 1993; *Knackstedt et al*., 2001], leads to a more gradually-varying capillary pressure-saturation relation [*Rajaram et al*., 1997; *Mani and Mohanty*, 1999], and improves connectivity and hence relative permeability of both phases [*Mani and Mohanty*, 1999]. Changes in fluid retention were also observed upon varying the correlation length of particle wettability in a bead pack [*Murison et al*., 2014].

Here, we present a systematic investigation of the impact of spatial correlations in particle size on the drying rate and patterns in porous media. We use pore network modeling complemented with microfluidic experiments to obtain a rigorous quantitative analysis and improve our understanding of the underlying mechanisms. We show that increasing the correlation length promotes preferential invasion, hence preserving liquid connectivity and surface wetness, delaying the transition between the drying stages.

2. Methods

One of the main challenges in studying fluid displacement processes such as drying is their large sensitivity to pore-scale details [*Bultreys et al*., 2016]. This sensitivity typically requires multiple realizations for each set of conditions in order to obtain a statistically-representative description [*Mani and Mohanty*, 1999]. Here, we formulate a minimal model which describes the essential pore-scale physics of this process—including evaporation from interfaces, vapor diffusion, and capillary invasion—via a set of simple rules for interactions between pores. We use this model in computer simulations to generate a sufficiently-large data set to overcome this sensitivity. We further validate our model using microfluidic devices with state of the art manufacturing and measurement resolution.

As we seek fundamental understanding of the underlying mechanisms of drying in heterogeneous porous media, rather than an accurate quantitative description of specific materials, we choose a simplified analog of a disordered porous medium as our model system. In particular, we use an array of cylindrical solid pillars (our particles) placed on a regular square lattice, where heterogeneity is achieved by varying the pillar radii (Figure 1). We note that both our experimental and numerical methodologies allow use of other designs, such as a triangular lattice or a random close packing. We consider here a horizontal sample, to avoid gravitational effects. We also do not model liquid films, since for our pore geometry–unlike systems such as networks of channels or granular media–such films are not expected to be well-connected (further discussion and supporting evidence are provided in section 4.1.1). The sample is open to the atmosphere at one of its faces, from which vapor diffuses outside and air invades into the medium (Figure 1a). Our model is described below, together with a brief description of our microfluidic experiments. Further details of our

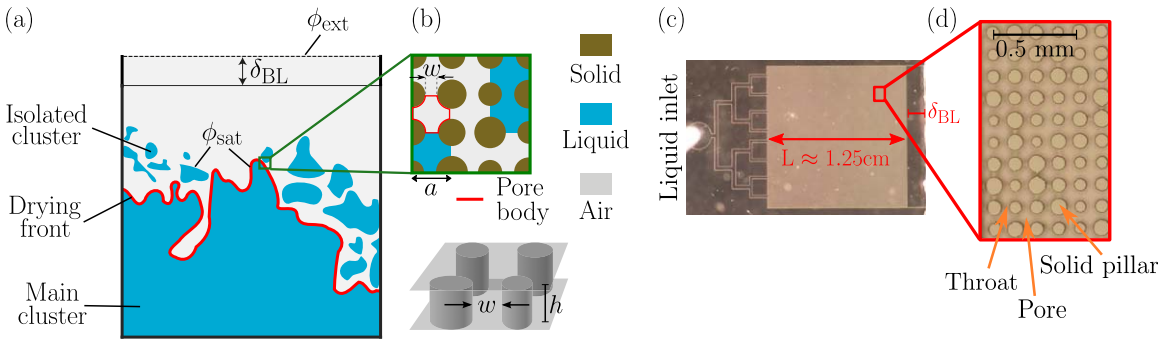

Figure 1. (a) Schematics of our model of isothermal drying of a horizontal porous sample open to the atmosphere at one of its faces. Low vapor concentration ($\phi=\phi_{ext}$) at the edge of a diffusive boundary layer (of thickness δ_{BL}) that develops outside the medium drives evaporation and vapor diffusion away from air-liquid interfaces (where $\phi=\phi_{sat}$). Evaporation reduces liquid pressure, causing air to invade into liquid-filled pores. Some of the liquid disconnects from the bulk (i.e., the main cluster) and becomes isolated. The drying front, namely the leading part of the air-liquid interface (excluding isolated clusters), is marked in red. (b) We model evaporation, vapor diffusion and capillary invasion via a pore network model. Pores are defined as the space (delimited by a red line) between solid pillars (constant height h and variable radius R) placed on a square lattice (spacing a), and are interconnected by throats (aperture w). (c) Drying experiments are performed in a horizontal microfluidic cell, initially filled with a volatile liquid via inlet channels. A boundary layer forms within an open region (pillar-free) of thickness δ_{BL}. (d) Close-up image showing the solid cylindrical pillars (top view).

experiments and a discussion of the ability of such a minimal model to capture the experimental behavior appear in a companion paper, [*Fantinel*, 2017; see also https://arxiv.org/abs/1612.01897].

2.1. Pore Network Model

We develop a pore-network model of a drying porous medium, discretizing the pore space into individual pores (the space between four neighboring pillars) connected by throats (the constrictions between two adjacent pillars; Figure 1b). Drying has been simulated using pore network models for more than two decades [*Nowicki et al*., 1992; *Prat*, 1993; *Tsimpanogiannis et al*., 1999]; for a review see e.g., *Prat* [2002, 2011]. We extend our pore-network to include vapor diffusion in the air boundary layer above the medium's open surface, by discretizing this region into interconnected "cells" as in *Laurindo and Prat* [1998]. This layer represents the atmospheric demand of vapor, which sets the potential rate of evaporation from the porous media. We capture the two-dimensional (2-D) distribution of vapor concentration which develops in the boundary layer as the surface dries [*Suzuki and Maeda*, 1968; *Yiotis et al*., 2007; *Shahraeeni et al*., 2012] (for further details see supporting information).

The evaporation rate is computed from the rate of vapor diffusion away from air-liquid interfaces. Vapor concentration and fluxes are resolved in the entire domain—air-filled pores as well as boundary layer cells—from the conservation of mass of vapor. A further simplification is provided by the much longer timescale of vapor diffusion, relative to the timescales of interface advancement and filling of a newly invaded pore with vapor. Based on the separation of these timescales, we can represent the dynamics of the air-liquid interface as a sequence of steady-state configurations, excluding the transient evolution of vapor concentration following interface advancement from our model. With this, vapor concentrations are obtained by enforcing the continuity equation in each pore (or boundary layer cell) i,

$$\sum_j J_{ij}A_{ij}=0 \tag{1}$$

where the summation is done over all neighboring pores (or cells) j. Here

$$J_{ij}=-\rho_v^{sat}D\nabla\phi|_{ij} \tag{2}$$

is the vapor mass flux between two adjacent pores i and j, driven by the local gradient of relative vapor concentration, $\nabla\phi|_{ij}=(\phi_j-\phi_i)/l_{ij}$, where $\phi=\rho_v/\rho_v^{sat}$ is the local vapor density ρ_v normalized by the saturated vapor density ρ_v^{sat}, and D is the binary diffusion coefficient of vapor in air. Throat ij, connecting pores i and j, has an effective cross-sectional area of $A_{ij}=\alpha w_{ij}h$, where $w_{ij}=a-R_I-R_J$ (R_I and R_J are the radii of pillar of that throat, i.e., for boundary layer cells $w_{ij}=a$) is its aperture and h is the pillar height (the out-of-plane sample thickness). The coefficient α accounts for the variable pore width (varying between w at the throat and a at the pore's center); a value of $\alpha=1.6$ was determined for our pore geometry by finite-element simulations at the subpore scale. In the boundary layer, the effective aperture corresponds to the full width of the cell, i.e.,

$\alpha = 1$. The distance l_{ij} is taken to be the lattice spacing a if both pores are air-filled, and in boundary layer cells. For an air-filled pore i along the air-liquid interface, we set $\phi_j = \phi_{sat} = 1$ as a boundary condition for the diffusion problem, where J_{ij} represents the local evaporation rate from interface ij, with $l_{ij} = a/2$. Other boundary conditions are fixed concentration, $\phi = \phi_{ext} = 0$, at the external edge of the diffusive boundary layer, and no-flux ($J = 0$) conditions at all cell faces not open to the atmosphere. This provides a set of coupled linear equations in terms of ϕ in each pore and boundary layer cell.

Invasion of air into liquid-filled pores depends on the local capillary pressure, or equivalently, the meniscus curvature (where the two are related via the Young-Laplace law). We relate the change in curvature to changes in liquid volume by approximating each throat as a cylindrical capillary tube with an effective radius of $r_{ij}^* = \left(1/h + 1/w_{ij}\right)^{-1}$, with a spherical meniscus of curvature C, such that invasion would occur once the critical curvature for throat ij, $C_{ij}^* = 2/r_{ij}^*$, has been exceeded, $C \geq C_{ij}^*$. This approximation of C_{ij}^* is ~5% higher than that calculated from the Mayer-Stowe and Princen method [*Lago and Araujo*, 2001, equation (55)], a minor difference that should not appreciably affect our results. Consequently, the curvature of a meniscus C is linked to the liquid volume evaporated from it, ΔV_{ij}, by

$$\Delta V_{ij} = \frac{\pi (2/C)^3}{3}\left(1 - \sqrt{1 - \left(C/C_{ij}^*\right)^2}\right)^2 \left(2 + \sqrt{1 - \left(C/C_{ij}^*\right)^2}\right) \tag{3}$$

where ΔV_{ij} is the total volume decrement relative to a flat meniscus (where $C = 0$), which is equal to the sum of the incremental changes in the volume of meniscus ij prior to the current time. The incremental volume change for a time step Δt is $\Delta t J_{ij} A_{ij}/\rho_l$, where ρ_l is the liquid density. The volume of a pore is $\left(a^2 - \pi \sum_l R_l/4\right)h$, where I is the index of the four pillars enclosing it (Figure 1b). Further details of the derivation of equation (3) appear in Appendix A.

To resolve the curvatures of all menisci from the evaporated volume, we use the following closure relations: (1) the total liquid volume decrement from any cluster equals the sum of volumes decreased from all menisci ij in that cluster, $\Delta V_{tot} = \sum_{ij} \Delta V_{ij}$; and (2) this deficit is divided between the cluster's menisci such that their curvature C remains uniform (for all throats). The latter is justified by the much faster pressure diffusion in liquid than vapor diffusion in air, allowing us to consider instantaneous liquid pressure equilibration. Once a pore is invaded, the liquid volume associated with it is redistributed to other interfacial pores in that cluster, decreasing the cluster's curvature C according to equation (3). Since C is uniform, every meniscus can receive a different volume (according to the corresponding throat radius, r_{ij}^*). We restrict the volume of liquid that can be redistributed by enforcing $C \geq 0$; we consider a pore completely dry and advance the interface only once all of its liquid is either redistributed, or, if limited by $C \geq 0$, evaporated.

Simulations begin with a liquid-saturated sample. Our computational algorithm is as follows: (i) The evaporation rates from the air-liquid interfaces, for a given interface configuration (invasion pattern), are computed from equations (1) and (2); (ii) The time-step until the next invasion event is calculated. This is the time required to reach the minimal evaporated volume (ΔV_{tot}) corresponding to a meniscus curvature sufficient to invade a throat, determined via equation (3); (iii) The interface configuration is updated once the invaded pore empties completely (instantaneously, unless redistribution is restricted). The process is then repeated by returning to step (i), until we reach breakthrough or a desired saturation.

2.2. Generating Correlated Geometries

For both experiments and simulations we generate samples in which the solid pillar sizes are locally correlated, that is where small pillars are more likely to be found next to other small pillars, and vice versa. The samples are generated according to the following protocol: we construct a random Gaussian surface with a prescribed spatial correlation length ζ (measured in units of the lattice spacing a). We then sample this surface on the grid of pillars, and use these values to determine the pillar sizes.

In particular, the random rough surface $H(x, y)$ is generated by noting that its Fourier transform should be a Gaussian distribution of intensities, centered around zero, with random phases. This Gaussian distribution is prepared by summing a thousand sine waves, whose amplitude, phase, and orientation were selected from a random uniform distribution, and whose wave numbers were drawn from a normal distribution. The width of this distribution, in Fourier space, is inversely proportional to the correlation length ζ of the surface. For a review of methods to generate rough surfaces see *Persson et al.* [2005]. We then transform this from a

normal to a uniform distribution by mapping the cumulative distribution function of the random rough surface onto the range $H(x,y) \in [-\lambda, +\lambda]$ where λ is a measure of the heterogeneity in pillar sizes. Finally, the radius R_l of each pillar is chosen as $\bar{R}(1+H_l)$, where $H_l=H(x_l, y_l)$ is the height of the surface at the center of that pillar (coordinates x_l, y_l). An overbar denotes an arithmetic average throughout the text.

The following parameter values were used in both simulations and experiments: sample size of 100 $\times$ 100 pillars, with $\bar{R}=50$ μm, $a=130$ μm, $\bar{w}=30$ μm, and $h=40$ μm, providing a mean porosity of 0.53. For the completely uncorrelated samples ($\zeta=0$), slightly different values of $a=125$ μm and $\bar{w}=25$ μm were used (porosity of 0.5). We generated two sets of data for this paper: (i) a large set for statistical analysis (simulations only); and (ii) a smaller set for comparison between simulations and experiments. Statistics, including ensemble averages and deviations, were obtained from a set of 40 realizations (namely samples with different random seeds) for each ζ, with ζ values of 0, 1, 1.5, 2, 2.5, 3, 4, 6, 10, and 15 (a total of 400 simulations), $\lambda=0.1$, and $\delta_{BL}=2$ mm. Comparison of simulations and experiments was performed in samples with identical pore geometry, using 8 correlated samples (ζ values of 1, 4, 10, and 15, normally-distributed sizes with λ values of 0.1 and 0.2) and 8 uncorrelated samples ($\zeta=0$, and λ values of 0.03, 0.05, 0.1 and 0.2). Due to the formation of sample-spanning patches for $\zeta=15$, potentially introducing sample-scale effects, we do not include these simulations in the quantitative analysis along with other ζ values. For completeness, comparison between experimental and simulated patterns for all ζ values, including $\zeta=15$, is provided in the supporting information.

2.3. Microfluidic Experiments

Micromodels made of an array of cylindrical pillars in between two planar plates are manufactured using standard microfluidic (aka "lab-on-a-chip") techniques including soft lithography. For further details see *Fantinel* [2017]. Briefly, a silicon wafer is spin-coated with a negative photoresist (SU8 3025, MicroChem Corp.), which is then exposed to UV light through a mask to produce the desired design (pillar positions and sizes). After rinsing, the remaining SU8 structure is used as a primer for a secondary mold of polydimethilsyloxane (PDMS). The PDMS is then cured and is used as a mold for the final sample, made of Norland Optical Adhesive 81 (NOA, Sigma-Aldrich). The NOA sample is then cured and exposed to white light to stabilize its optical properties. Our manufacturing procedure resolution is $\sim$2 μm, with an estimated uncertainty in pillar sizes of $\sim$1.6 μm ($\sim$3.2% of design). The potential impact of such uncertainty is discussed in section 4.1.2.

A boundary layer is included in the experimental design by leaving the region adjacent to the open side empty of solid pillars (Figure 1c). Uncertainty introduced by variations in the experimental layer width δ_{BL} (2 ± 1 mm), and possibly its extension into the air immediately outside of the open edge of our cell, lead to a range of initial rates for similar experimental layer width δ_{BL}. Thus, to compare rates we use in the simulations an effective value for δ_{BL}, computed by matching the initial experimental rates, as in *Vorhauer et al.* [2015]. A sensitivity analysis showing how uncertainty in δ_{BL}, impacts drying appears in [*Fantinel*, 2017; see also https://arxiv.org/abs/1612.01897].

The sample is initially filled with a fluorinated oil Novec 7500 [*3M*, 3M Electronics Materials Solutions Division, St. Paul, MN, 2016] through inlet channels (Figure 1c). At the experimental temperature ($25\pm1^{\circ}$C), the fluid properties are: vapor pressure of $2.1\cdot10^3$ Pa, $\rho_v^{sat}=0.35$ kg/m^3, interfacial tension of $\gamma=0.0162$ N/m [*3M*, 2016], and $D=5\cdot10^{-6}$ m^2/s [*United States Environmental Protection Agency*, USEPA Ecosystems Research, Athens, GA, 2016]. The cell, placed horizontally to avoid gravitational effects, is left to dry under a digital SLR camera (Nikon D5100) with a macro lens. Illumination is provided by a ring of LEDs surrounding the cell. Time-lapse images are taken every minute, with a spatial pixel resolution of 5 μm, equivalent to a liquid mass on the order of 1 nanogram (providing here a more accurate method for monitoring drying progression over weighting). Experiments are stopped at breakthrough, since past breakthrough air can invade the inlet channels.

Our image analysis procedure is briefly described below (for further details, see *Fantinel* [2017]). First, the red color channel of the image, which contains the best contrast, is extracted. Then, a bandpass filter is applied to remove both the high-frequency noise and any low frequency variations in intensity. Subtraction of the first image from each image sequence removes constant sources of background noise. Thresholding then provides a binary image with wet (white) and dry (black) areas. Finally, we remove the solid pillars to obtain a continuous distribution of liquid and air. Drying rates are computed from the difference in the dry area between consecutive time-lapse images. To reduce the noise introduced by such operation, the resulting rates are filtered with a low-pass filter with a cutoff of 0.1 (i.e., smoothing over 10 images), and further

averaged with a 5-point moving average. To compare with simulations we also generate a discrete data set of the invasion time for each pore by identifying the locations of the pores and their occupancy throughout the time-lapse sequence of images.

3. Results

3.1. Comparing Model With Experiments

3.1.1. Drying Patterns

Our simulated drying patterns agree well with the corresponding patterns in microfluidic experiments using identical pore geometries (Figure 2a; additional patterns are provided as supporting information). The match between a pair of patterns is defined here as the number of overlapping invaded pores (common to both patterns) divided by the average number of invaded pores, at breakthrough (see Appendix B). Comparison of all our experimental patterns versus the respective simulations (namely pairs of similar pore geometry) provides an average match of 59%, with a standard deviation of 19% from that mean. Other metrics, including the front roughness and the main cluster saturation, are also in agreement [*Fantinel*, 2017]. An exception is the Euler number—the invading phase connectivity computed as the number of clusters of air-filled pores minus the number of liquid clusters ("islands") within them–which does not (in some cases the experimental values reach -200 whereas simulations do not exceed -70 [*Fantinel*, 2017]). This disparity is due to isolated liquid clusters that form and persist for longer periods in the experiments (see videos in supporting information). Accordingly, when considering the leading front (ignoring small isolated clusters, as often done to estimate finger width [*Toussaint et al*., 2012]), the pattern match improves (average of 64% with a standard deviation of 22%).

3.1.2. Drying Rates

Our simulated drying rates are generally in good agreement with experiments, except for later stages (at low saturations), where simulations exhibit fewer isolated clusters near the surface. The disappearance of near-surface isolated clusters forces the drying front to recede deeper into the medium, and the simulated rate to drop (Figure 2b). Here, e is the evaporative flux, in terms of volume of liquid evaporated per unit time and area of open surface, and S is the saturation, computed as the ratio between the liquid volume remaining and the total pore volume. We note that the experimental rates exhibit fluctuations, and at times a lack of a well-defined constant rate period (Figure 2b, and supporting information Figure S2). Such noise is a consequence of evaluating the rates from the time-lapse images, and also conceivably changes in the air circulation in the laboratory.

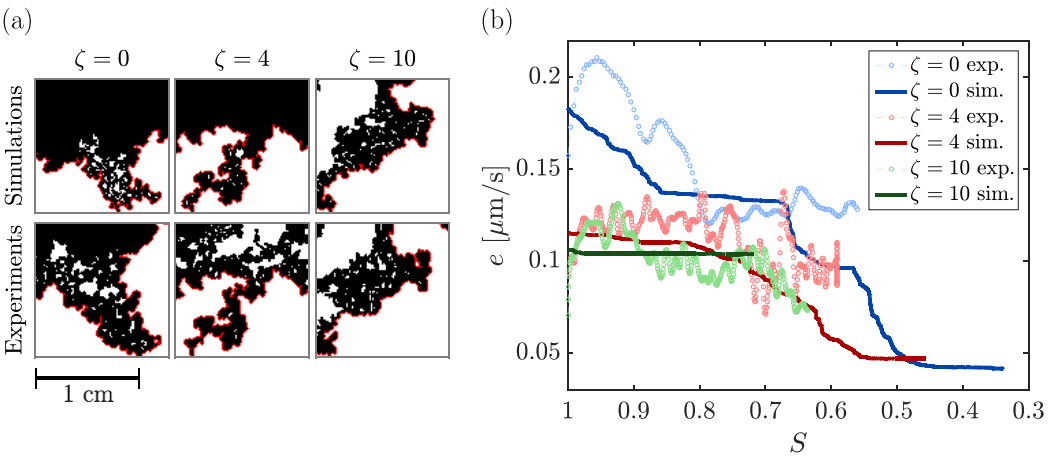

Figure 2. (a) Simulated and experimental patterns for samples with different correlation length, ζ, are in good agreement. The main difference is the persistence of near-surface isolated clusters for longer periods experimentally. Black and white denote pores filled with air and liquid, respectively (solid not shown); the red line indicates the drying front. The sample size (pore space only) is ~1.25 cm. (b) Simulated drying rates e initially follow the experimental ones, however they show a faster rate drop at lower liquid saturation, S (the ratio between the liquid volume and the total pore volume). This drop is associated with reduced persistence of isolated clusters in simulations, pushing the drying front deeper, and thus lowering the drying rate.

Since vapor saturations and evaporation rates are a consequence of the liquid distribution, disagreement in patterns would jeopardize the match in rates. To further examine the impact of the drying pattern on rate, we computed the *theoretical* rates (using equations (1) and (2)) from the observed experimental patterns, by solving Laplace's equation for the pore-by-pore sequence of experimental patterns. These rates match well the experimental ones (see supporting information Figure S3). This suggests that the disparity in patterns is responsible for that in rates; it also confirms the validity of our evaporation and vapor transport calculations.

3.2. Impact of Spatial Correlation

3.2.1. Drying Patterns

Our simulations demonstrate that increasing the correlation length ζ enhances the connectivity of pores of similar size, and hence the accessibility of larger pores across the sample. This promotes preferential drying of larger pores while smaller pores remain wet and maintain liquid connectivity to the surface. As a result, increasing ζ forces the drying patterns to follow more closely the underlying pore geometry (Figure 3a). Similarly, the tendency to invade larger pores, quantified here by the fraction of larger-than-average invaded pores, χ_L, increases with ζ (Figure 3b; see Appendix C for the evaluation of χ_L). Another consequence of preferential drying is that it reaches deeper parts of the medium, leading to an earlier breakthrough, as demonstrated by the increase in the invasion depth $\overline{Z_0}$ with ζ (Figure 3c). Here $\overline{Z_0}$ is the depth of the center of mass of the invaded pores (marked in gray in Figure 3a).

3.2.2. Drying Rates

Maintaining liquid connectivity in more correlated samples preserves surface wetness, which, due to its strong influence on drying rates, prolongs stage 1 and delays the rate drop marking the onset of stage 2 [*Lehmann et al.*, 2008; *Shokri et al.*, 2010; *Shahraeeni et al.*, 2012]. Our simulations capture the more gradual decrease in surface wetness, as demonstrated here via a slower drop in surface saturation S_{surf} (the liquid saturation for the row of pores closest to the boundary layer) with overall liquid saturation S in samples with longer correlations ζ (Figure 4a). This results in faster drying, as shown by: (i) maintenance of higher

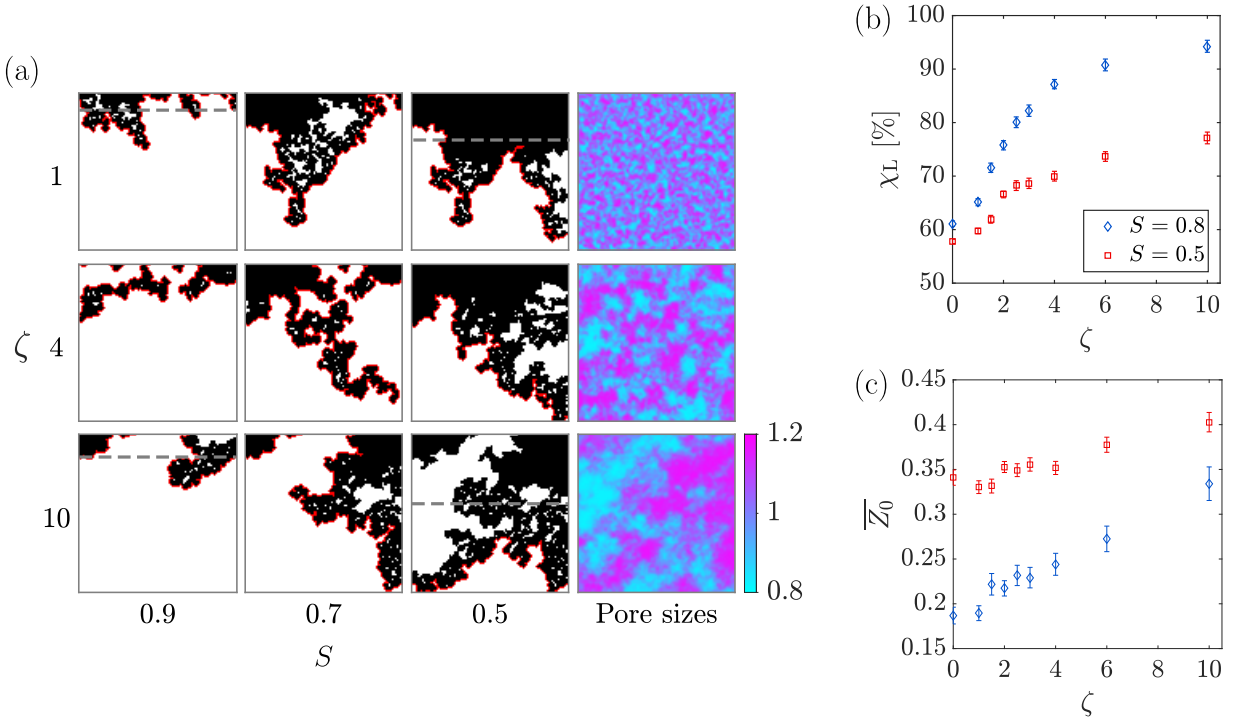

Figure 3. (a) Our simulations show that increasing correlation length ζ (in units of lattice spacing a), promotes preferential drying of connected large pores, such that the drying pattern follows more closely the underlying sample geometry. Patterns at different liquid saturation, S, are shown next to the pore size distribution (in terms of volume, normalized by the mean; purple indicates large pores). The tendency for preferential drying, quantified here through (b) the fraction of larger-than-average invaded pores, χ_L, and (c) the mean invasion depth, $\overline{Z_0}$ (marked by a gray line on a few patterns in panel a), increases with ζ. Symbols and bars in Figures 3b and 3c represent ensemble average and standard error from 40 realizations, for S=0.5 and S=0.8.

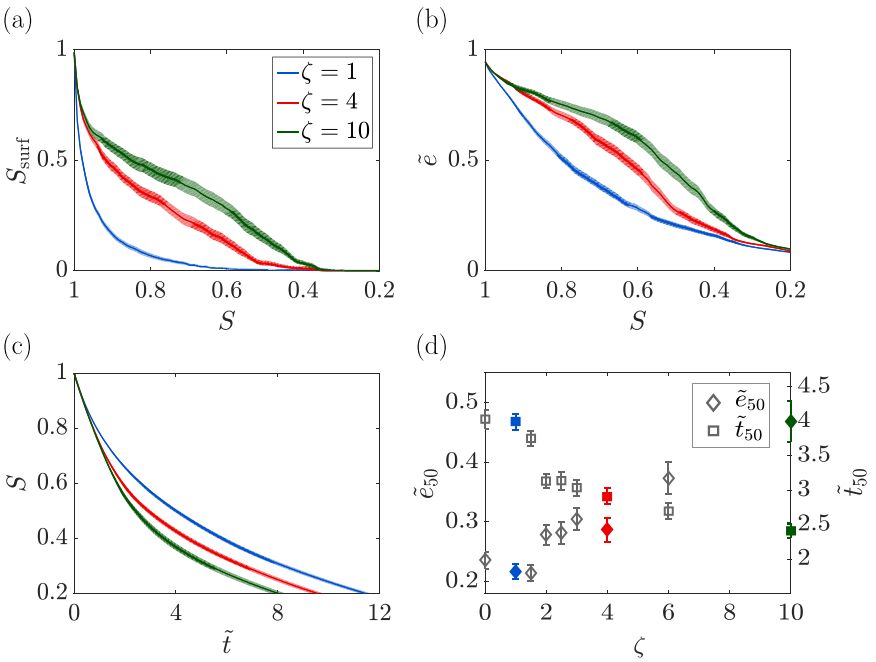

Figure 4. Increasing correlation length ζ maintains liquid connectivity to the surface, (a) prolonging higher surface wetness, S_{surf}, and (b) faster drying rates, $\tilde{e}$, for longer duration, such that (c) the saturation S drops faster with time $\tilde{t}$. (d) Quantitatively, increasing ζ increases the rate at $S = 50\%$, $\tilde{e}_{50}$ and decreases the time to reach $S = 50\%$, $\tilde{t}_{50}$. For each ζ we plot the ensemble average (lines in Figures a–c; symbols in Figure 4d where colors highlight ζ of 1, 4, and 10.) and standard error (shading in Figures 4a–4c, error bars in Figure 4d) from 40 realizations.

rates $\tilde{e}$ for longer duration (lower S, Figure 4b); and (ii) faster decline of S with time $\tilde{t}$ (Figure 4c). We use the following nondimensional rate and time: $\tilde{e}=e/e_0$ where $e_0=(\rho_v^{sat}/\rho_l)D\phi_{sat}/\delta_{BL}$ is the potential drying rate, and $\tilde{t}=t/t_0$ where $t_0=nL/e_0$ is the characteristic time to evaporate liquid from a sample of depth L and porosity n. The enhancement of the drying rate by increasing ζ is further quantified through the larger rate at $S=50\%$, $\tilde{e}_{50}$, and shorter time to reach $S=50\%$, $\tilde{t}_{50}$ (Figure 4d).

4. Discussion

4.1. Predictive Model Capabilities: Simulations Versus Experiments

Our simulated patterns are generally in good agreement with microfluidic experiments using similar pore geometry, as quantitatively shown through the agreement in pattern match, front roughness and main cluster saturation [*Fantinel*, 2017]. The main differences between simulated and experimental patterns are the reduced formation and persistence of isolated clusters in the simulations, and the earlier rate drop compared to the experiments. We note that the experimental leading front (the pattern excluding isolated clusters) is well captured by our simulations. In fact, our ongoing work shows that the leading front can be predicted by an invasion percolation (IP) model; however, we use here a more involved model since IP ignores two aspects which are crucial to the current work: (i) drying of trapped clusters and (ii) dynamics (e.g., IP, being quasi-static, ignores time which is required to determine rates). Potential sources for the aforementioned discrepancies include liquid films, wettability effects, and uncertainty in pore geometry; their impact is discussed below.

4.1.1. Liquid Films and Wettability Effects

Liquid films can provide a source of liquid for isolated clusters close to the open surface, thus delaying invasion into these clusters and maintaining higher drying rates at lower saturations. In systems such as etched (channel) networks or granular media, such films can persist in channel corners, rough surfaces, and interstices between neighboring particles [*Laurindo and Prat*, 1998; *Prat*, 2011; *Yiotis et al.*, 2012]. For our pore geometry, the liquid capillary rings around solid pillars that remain after a pore is invaded are not expected to be well-connected, with little effect on liquid connectivity. This hypothesis is supported by optical microscope images from our microfluidic experiments, showing different meniscus curvatures and hence capillary pressures in adjacent isolated liquid clusters.

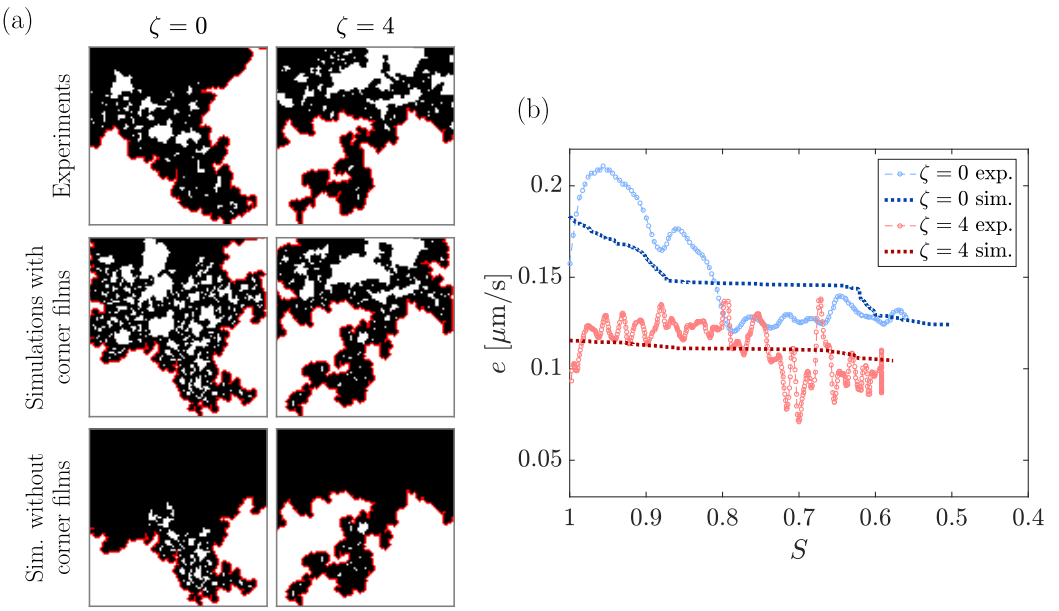

Figure 5. We evaluate the potential impact of liquid films in the corners at the cell's outer edges by simulating films which extend throughout the entire cell including the boundary layer, and during the entire experiment. Introducing these films prolongs the persistence of (a) isolated clusters close to the open side and (b) faster drying rates; bottom row in Figure 5a shows simulated patterns without films (from Figure 2). Black and white denote pores filled with air and liquid, respectively (solid not shown); red line indicates the drying front.

In our experiments, however, films at the corners of the cell's edges may enhance connectivity between the main liquid reservoir and the open surface, hence promoting evaporation from depth on the expense of isolated clusters closer to the surface. To evaluate the potential effect of this mechanism, we simulate a scenario in which these films extend throughout the entire cell (including the part without solid pillars, i.e., the boundary layer), and during the entire experiment. This is crudely represented by enforcing wet pores along the two cell edges (numerically, fixing a value of ϕ=1 in all pores and boundary layer cells along these edges) throughout the simulation. In these simulations, persistence of isolated clusters close to the open side and faster drying rates are maintained for longer periods (compared to simulations without corner films; Figure 5). These simulations also exhibit a more distinctive constant rate period, which could be explained by the presence of liquid films at the cell's corners. We stress that these simulations overestimate the effect of such films (regardless of the details of their geometry), since they are expected to shrink and recede deeper into the cell during the experiment; indeed, both the isolated clusters and the high initial rates in these simulations persist longer than in the experiments (Figure 5).

The reduced formation of isolated clusters could also be attributed to wettability effects. To examine the impact of wettability, we compare our experiments with highly-wetting oil (contact angle of $\sim 3^\circ$ [*3M*, 2016]) with one using water ($\sim 70^\circ$ [*Silvestrini et al*., 2012]). The two experiments mainly differ by the number of isolated clusters formed, suggesting that wettability effects, which are not included in our model, could decrease the agreement between our simulations and experiments [*Fantinel* 2017; see also https://arxiv.org/abs/1612.01897].

4.1.2. Uncertainty in Pore Geometry

An inevitable source of disparity in patterns, and consequently in rates, is manufacturing errors (referred to here as "noise") introducing uncertainty in pore geometry. Our state-of-the-art manufacturing procedure provides small random errors in pillar radius, of $\sim$1.6 μm, corresponding to $\sim$3.2% of the mean. The emergent patterns—in drying, and, in general, immiscible displacement—are highly sensitive to small geometrical details; that is, slight changes in pore sizes, even locally, can significantly alter the pattern [*Bultreys et al*., 2016]. An extreme example of this sensitivity is the "binary choice" that can occur when the invasion front reaches a bottleneck in the form of a narrow throat; if slightly altered, the invasion may proceed elsewhere, bypassing an entire region. Such a case is presented in the supporting information (supporting information Figure S2, λ=0.2, $\zeta = 15$), showing distinctively different patterns in experimental samples made from the same mold (identical *design*).

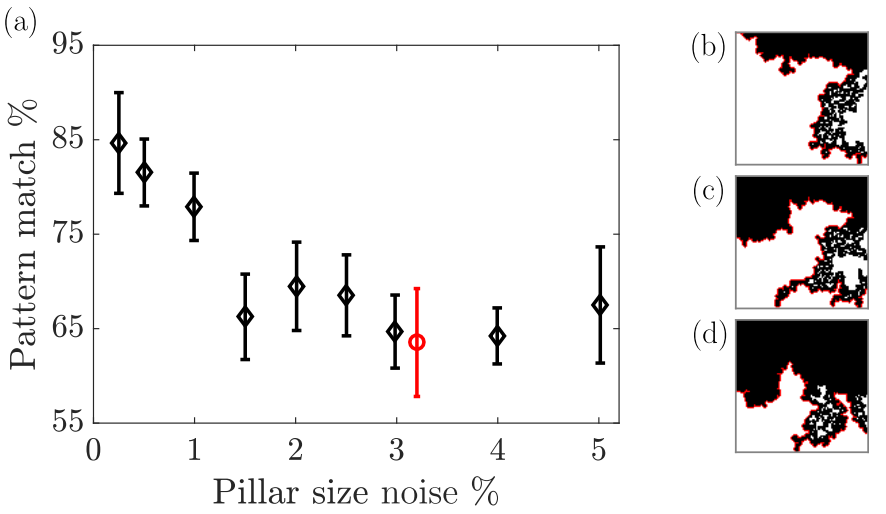

Figure 6. To evaluate the impact of geometrical uncertainty, we introduce random noise in pillar sizes in the simulations, mimicking manufacturing errors. Significant changes to the emergent drying patterns demonstrate their sensitivity to small geometrical details. (a) Our simulations show a reduction in pattern match from ∼85% to ∼65% (at breakthrough) as the noise increases from 0.25% to 1.5% (in black, symbols and bars are ensemble averages and standard errors from 10 samples with $\zeta = 0$). Given the experimental uncertainty in pillar sizes (∼3.2%), our simulated patterns agree very well with the experiments (in red, for $\zeta = 0$). The sensitivity to details is exemplified by the alteration of the drying pattern of a particular sample (b) caused by introducing an error of 1% (c) and 3% (d), reducing the match from 77% to 65%, respectively.

To quantify the sensitivity of the drying pattern to perturbations in pore geometry, we introduce, numerically, random noise in pillar sizes. Simulations with different noise values (applied to 10 different samples) show that the pattern match at breakthrough drops to ∼65% when the error reaches 3% (Figure 6a). The fact that we obtain a comparable match between simulations and experiments indicates that our model predicts patterns very well within the experimental uncertainty in pillar sizes (∼3.2%, cf. Figure 6a). To exemplify the impact of uncertainty in geometry, we show how increasing the noise introduced to a specific sample design (Figure 6b) from 1% to 3% reduces the pattern match at breakthrough from 77% to 65% (Figures 6c and 6d, respectively).

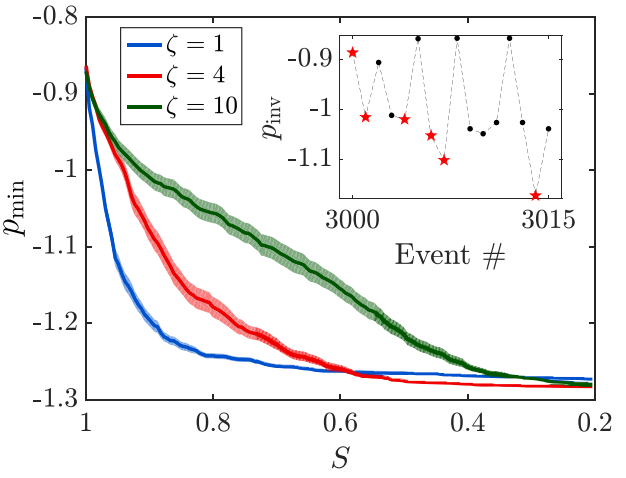

Figure 7. In more correlated media (higher ζ), improved connectivity and preferential drying of large pores results in a more gradual change in the critical (minimum) invasion pressure, p_{min}, as drying proceeds (with decreasing saturation, S). That is, a large number of pores can be invaded without a significant increase in capillary pressure (decrease in liquid pressure). Here p_{min} is an extreme value of the minimal pressure recorded among all liquid-filled pores during an invasion event, p_{inv}, since the beginning of the simulation. An example of how p_{min} is computed is provided in the inset, showing the minimal liquid pressures p_{inv} for a series of 16 invasion events from a specific simulation: new (record-low) minima are marked by red stars, other events (local minima) by black dots. The main panel shows values of p_{min} versus saturation from 40 realizations (lines and shading are ensemble average and standard error).

4.2. Impact of Correlation Length

4.2.1. Pressure Evolution

The tendency to preferentially invade large pores, which increases with correlation length, also affects the evolution of the liquid pressure. Each time the invasion front reaches a narrower throat, a further decrease in liquid pressure (by evaporation) is required to overcome the large capillary threshold. In a medium with noncorrelated heterogeneity, the frequency of such events is high; in contrast, the interconnectivity of pores of similar sizes at high ζ reduces the frequency of such events, as exceeding a threshold enables invasion of multiple pores. Indeed, in samples with lower ζ we observe a sharper

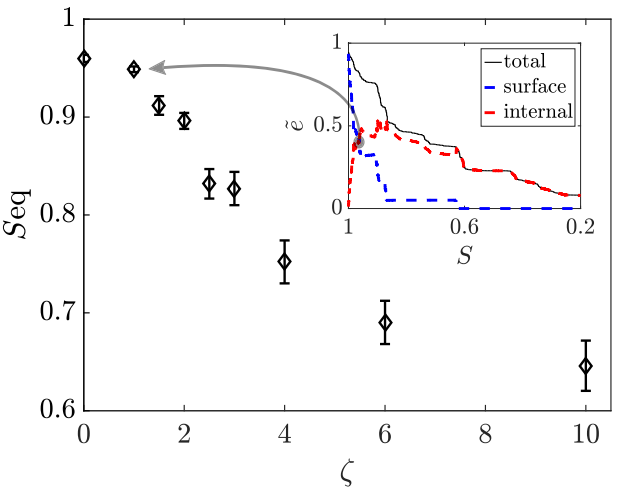

Figure 8. The transition between the drying stages is delayed (i.e., it occurs at smaller liquid saturations) as the correlation length ζ increases. The transition is defined here as the saturation at which the evaporation rate from surface pores equals that from internal pores, S_{eq}. Diamonds and bars are ensemble average and standard error from 40 realizations. The inset shows the breakup of evaporation rates for a sample with $\zeta = 1$; the crossing of the red and blue lines provides S_{eq}.

drop in the minimum pressure p_{min} with saturation S (Figure 7); that is, the capillary pressure required for the front to advance becomes larger as drying proceeds and S decreases, in accordance with observations from drainage simulations [*Rajaram et al.*, 1997]. Here p_{min} is an extreme minimal liquid pressure recorded since the beginning of the simulations, namely a record-low value of the minimal liquid pressure during an invasion event p_{inv} (see example in inset of Figure 7), normalized by a characteristic invasion pressure $p^* = 2\gamma(\bar{w}^{-1} + h^{-1})$.

4.2.2. Transition Between Drying Stages

Maintaining surface wetness through liquid connectivity to the open surface controls the transition between the different drying stages, that is between dominance of evaporation from the open surface, and from deeper parts of the medium's interior [*Lehmann et al.*, 2008]. Our pore-scale model allows us to quantify the relative strength of these mechanisms. We show that increasing spatial correlation delays this transition (Figure 8), defined here as the saturation at which the evaporation rate from the surface equals that from interior pores, S_{eq} (Figure 8, inset). We note that this analysis considers connectivity of liquid-filled pores only; this transition can be further delayed by enhanced connectivity of liquid to the open surface due to film flow along channel corners [*Laurindo and Prat*, 1998; *Chauvet et al.*, 2009] or intergranular contacts in particulate matter [*Shokri et al.*, 2010; *Yiotis et al.*, 2012]. Such a delay can be made evident in our simulations by evaluating the impact of films at the cell's outer edges (Figure 5). The ability to predict the point of transition between drying mechanisms could be exploited in practice; for instance, one could manipulate a material's microstructure to control the duration of stage 1 drying [*Assouline et al.*, 2014].

5. Conclusions

We study the impact of spatially-correlated pore geometry on isothermal drying of porous media. We present a minimal pore-scale model, describing evaporation, vapor diffusion, and capillary invasion by a set of simple rules for the interactions between pores. We compare our numerical simulations to state-of-the-art microfluidic experiments of similar pore geometry. Our simulated patterns compare favorably with the experiments, in light of the large sensitivity of the emergent patterns to uncertainty in pore geometry. We note the reduced formation and persistence of isolated clusters in simulations, leading to a faster drop in the evaporation rate than observed experimentally. Potential explanations for this discrepancy include film flow along corners at the sides of the cell, and wettability effects.

We find that increasing the correlation length promotes preferential invasion of large pores, which preserves liquid connectivity and surface wetness, maintaining higher drying rates for longer periods. We explain this behavior by quantifying the point of transition between dominant mechanisms (drying stages): from evaporation mostly at the surface, where rates are controlled by diffusion through the boundary layer, to evaporation from depth at a rate limited by the much slower vapor diffusion inside the porous medium.

Our approach of coupling a minimal pore-scale model with microfluidic experiments as a simple porous media analog could also be applied to study the effects of pore-scale heterogeneity in a wide range of problems including immiscible fluid-fluid displacement [*Holtzman*, 2016] and solute transport [*Kang et al.*, 2015]. Specifically, our findings improve our understanding of how pore-scale heterogeneity, inevitable in most porous materials, affects their drying rate and extent. These findings bear significant implications for

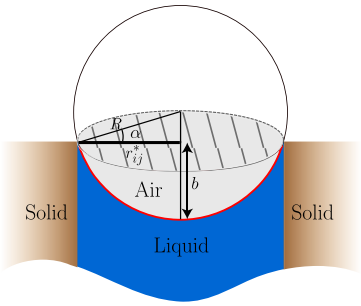

Figure A1. Schematics of our model relating the air-liquid meniscus curvature to the amount of liquid evaporated. A throat *ij* is represented as a cylindrical capillary tube with an effective radius of r_{ij}^*, with a spherical meniscus (red line) of curvature $C = 2/R$ where R is its radius. The volume evaporated since initial condition of zero curvature ($C = 0$), ΔV_{ij}, is the volume of the spherical cap (gray shading).

multiple industrial and natural processes, ranging from fuel cells [*Prat*, 2011], cements and paints [*Goehring et al*., 2015] to soil-atmosphere energy and moisture exchange and soil salinization [*Nachshon et al*., 2011; *Norouzi Rad et al*., 2013; *Or et al*., 2013].

Appendix A: Derivation of Liquid Volume-Meniscus Curvature Relation (Equation (3))

Our pore-scale model includes capillary invasion of air, once the critical entry threshold has been exceeded. At each time step, we update the capillary pressures (or equivalently, the meniscus curvature C, where the two are related via the Young-Laplace law) in each pore throat *ij* according to the amount of liquid evaporated during that step, ΔV_{ij}. To relate the change in curvature to changes in liquid volume, we approximate each throat as a cylindrical capillary tube with a radius of $r_{ij}^* = \left(1/h + 1/w_{ij}\right)^{-1}$ (Figure C1), where w_{ij} is the throat aperture and h is the pillar height (out of plane sample thickness). This allows consideration of a spherical meniscus of curvature C, and predict the onset of capillary invasion once the critical curvature for throat *ij*, $C_{ij}^* = 2/r_{ij}^*$, has been exceeded, $C \geq C_{ij}^*$.

With the above, the volume evaporated from the meniscus ΔV_{ij} (measured since the initial condition of zero curvature, $C = 0$) is related to its current curvature $C = 2/R$ through the spherical cap equation, $\Delta V_{ij} = \pi b^2(3R - b)/3$. Here R is the sphere radius, $b = R(1 - \sin\alpha)$ is the cap height and $\alpha = \cos^{-1}\left(r_{ij}^*/R\right)$ (Figure Figure C1). Replacing the radii r_{ij}^* and R with the equivalent curvatures and rearranging leads to equation (3).

Appendix B: Evaluating the Pattern Match

The pattern match $\Delta = N_{com}/N_{avg}$ between a pair of patterns is defined here as the number of overlapping invaded pores N_{com} (namely, the invaded volume common to both patterns, measured in number of pores)

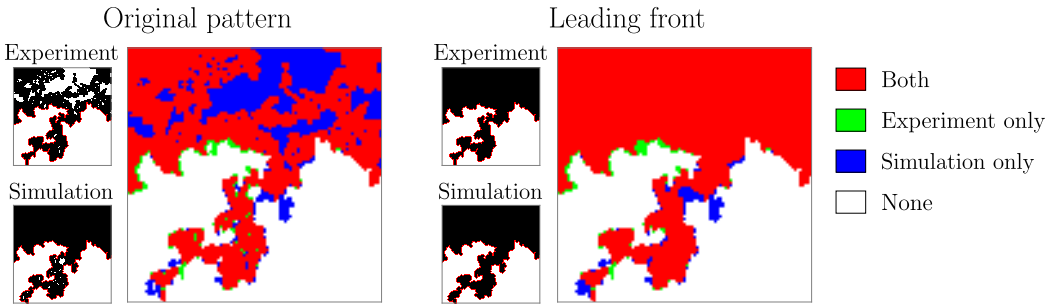

Figure B1. Calculation of the pattern match between an experiment and a simulation (same pore geometry) for the sample with $\zeta = 4$ and $\lambda = 0.2$. The match is calculated at breakthrough, for two pairs of patterns (shown as insets): (i) original patterns (left) and (ii) considering the leading front only (patterns modified by excluding the isolated liquid clusters, right). Images in the larger panels show invaded pores common to both patterns (in red), and pores invaded exclusively in the experiments (green) and in the simulations (blue). For each pair of patterns, the match is computed from the number of common invaded pores (red), divided by the average number of invaded pores in both patterns–the experimental (red+green), and the simulated (red+blue).

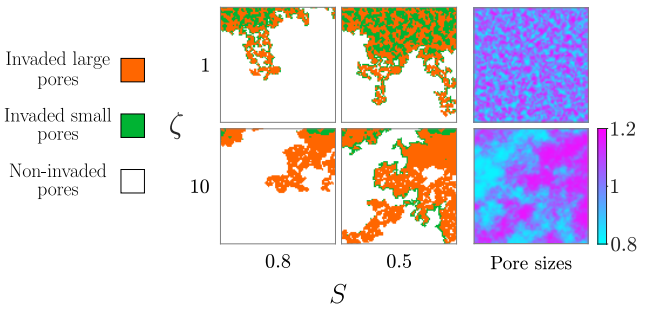

Figure C1. The fraction of larger-than-average invaded pores, χ_L, for two samples (ζ=1 and ζ=10) at two saturations (S=0.8 and S=0.5). The invasion patterns are segmented into invaded pores which are larger (orange) or smaller (green) than the mean (by volume); χ_L is the ratio of the number of larger pores over the total number of invaded pores. Pore size (in volume) for the two samples is shown in the rightmost plots.

divided by the average number of invaded pores in both patterns, $N_{avg}=(N_1+N_2)/2$. Here N_1 and N_2 is the number of invaded pores in each pattern. The match is evaluated at breakthrough of both runs, 1 and 2. In addition to the match between the original pair of patterns, we also compute the match considering the leading front (accounting for the main cluster only, excluding the isolated clusters).

An example of the evaluation of the match between an experiment and a simulation is provided in Figure Figure A1. For two pairs of patterns (in insets)–(i) the original pair (left) and (ii) the leading front (right), the invaded area common to both patterns appears in red, and the area invaded exclusively in the experiments and in the simulations appears in green and blue, respectively. The number of invaded pores for the original pair (left) is as follows: 4002 pores in the experiment, 5326 in the simulation, with 3859 overlapping, providing a match of 83%. Considering only the leading drying front (right) improves the match to 97%.

Appendix C: Computing the Fraction of Larger-Than-Average Invaded Pores

The fraction of larger-than-average invaded pores, χ_L (cf. Figure 3b), is defined as the number of invaded pores which are larger (by volume) than average (marked in orange in Figure B1), divided by the total number of invaded pores (orange+green). Figure B1 exemplifies this calculation for the two samples and two saturation values shown in Figure 3b: (i) for $\zeta = 1$, χ_L=62% (for S=0.8) and 56% (S=0.5); and (ii) for $\zeta = 10$, χ_L=93% (S=0.8) and 84% (S=0.5). The increase in χ_L with ζ demonstrates the increasing tendency to preferentially invade larger pores.

Acknowledgments
Financial support by the State of Lower-Saxony, Germany (#ZN-2823) is gratefully acknowledged. RH also acknowledges partial support from the Israeli Science Foundation (#ISF-867/13) and the Israel Ministry of Agriculture and Rural Development (#821–0137-13). Supporting information includes details of the derivation of equation (3), drying patterns from all microfluidic experiments with corresponding simulated patterns, and videos highlighting the dynamic evolution of the drying pattern in experiments and simulations. The data used are available by contacting the corresponding author.

References

3M (2016), *Heat Transfer Applications Using 3M Novec Engineered Fluids*. [Available at http://multimedia.3m.com/mws/media/1091997O/3m-novec-engineered-fluids-for-heat-transfer-line-card.pdf, last accessed 5 Apr. 2017.]

Assouline, S., K. Narkis, R. Gherabli, P. Lefort, and M. Prat (2014), Analysis of the impact of surface layer properties on evaporation from porous systems using column experiments and modified definition of characteristic length, *Water Resour. Res.*, *50*, 3933–3955, doi:10.1002/2013WR014489.

Bultreys, T., W. De Boever, and V. Cnudde (2016), Imaging and image-based fluid transport modeling at the pore scale in geological materials: A practical introduction to the current state-of-the-art, *Earth Sci. Rev.*, *155*, 93–128, doi:10.1016/j.earscirev.2016.02.001.

Chauvet, F., P. Duru, S. Geoffroy, and M. Prat (2009), Three periods of drying of a single square capillary tube, *Phys. Rev. Lett.*, *103*(12), 124502, doi:10.1103/PhysRevLett.103.124502.

Eijkel, J. C. T., B. Dan, H. W. Reemeijer, D. C. Hermes, J. G. Bomer, and A. van den Berg (2005), Strongly accelerated and humidity-independent drying of nanochannels induced by sharp corners, *Phys. Rev. Lett.*, *95*(25), 256107, doi:10.1103/PhysRevLett.95.256107.

Fantinel, P. (2017), Microfluidic cells as a model 2D granular material, PhD thesis, Georg-August University, Göttingen, Germany. [Available at https://arxiv.org/abs/1612.01897.]

Goehring, L., A. Nakahara, T. Dutta, S. Kitsunezaki, and S. Tarafdar (2015), *Desiccation Cracks and Their Patterns*, 368 pp., Wiley-VCH, Weinheim, Germany, doi:10.1002/9783527671922.

Holtzman, R. (2016), Effects of pore-scale disorder on fluid displacement in partially-wettable porous media, *Sci. Rep.*, *6*, 36221, doi:10.1038/srep36221.

Ioannidis, M. A., I. Chatzis, and E. A. Sudicky (1993), The effect of spatial correlations on the accessibility characteristics of three-dimensional cubic networks as related to drainage displacements in porous media, *Water Resour. Res.*, *29*(6), 1777–1785, doi:10.1029/93WR00385.

Kang, P. K., M. Dentz, T. Le Borgne, and R. Juanes (2015), Anomalous transport on regular fracture networks: Impact of conductivity heterogeneity and mixing at fracture intersections, *Phys. Rev. E*, *92*(2), 022148, doi:10.1103/PhysRevE.92.022148.

Knackstedt, M. A., A. P. Sheppard, and M. Sahimi (2001), Pore network modelling of two-phase flow in porous rock: The effect of correlated heterogeneity, *Adv. Water Resour.*, *24*(3–4), 257–277, doi:10.1016/S0309-1708(00)00057-9.

Lago, M., and M. Araujo (2001), Threshold pressure in capillaries with polygonal cross section, *J. Colloid Interface Sci.*, *243*(1), 219–226, doi:10.1006/jcis.2001.7872.

Laurindo, J. B., and M. Prat (1998), Numerical and experimental network study of evaporation in capillary porous media. Drying rates, *Chem. Eng. Sci.*, *53*(12), 2257–2269, doi:10.1016/S0009-2509(97)00348-5.
Lehmann, P., and D. Or (2009), Evaporation and capillary coupling across vertical textural contrasts in porous media, *Phys. Rev. E*, *80*(4), 046318, doi:10.1103/PhysRevE.80.046318.
Lehmann, P., S. Assouline, and D. Or (2008), Characteristic lengths affecting evaporative drying of porous media, *Phys. Rev. E*, *77*(5), 056309, doi:10.1103/PhysRevE.77.056309.
Mani, V., and K. K. Mohanty (1999), Effect of pore-space spatial correlations on two-phase flow in porous media, *J. Petrol. Sci. Eng.*, *23*(3–4), 173–188, doi:10.1016/S0920-4105(99)00015-7.
Metzger, T., and E. Tsotsas (2005), An influence of pore size distribution on drying kinetics: A simple capillary model, *Drying Technol.*, *23*(9–11), 1797–1809, doi:10.1080/07373930500209830.
Murison, J., B. Semin, J. C. Baret, S. Herminghaus, M. Schröter, and M. Brinkmann (2014), Wetting heterogeneities in porous media control flow dissipation, *Phys. Rev. Appl.*, *2*(3), 034002, doi:10.1103/PhysRevApplied.2.034002.
Nachshon, U., N. Weisbrod, M. I. Dragila, and A. Grader (2011), Combined evaporation and salt precipitation in homogeneous and heterogeneous porous media, *Water Resour. Res.*, *47*, W03513, doi:10.1029/2010WR009677.
Norouzi Rad, M., N. Shokri, and M. Sahimi (2013), Pore-scale dynamics of salt precipitation in drying porous media, *Phys. Rev. E*, *88*(3), 032404, doi:10.1103/PhysRevE.88.032404.
Nowicki, S. C., H. T. Davis, and L. E. Scriven (1992), Microscopic determination of transport parameters in drying porous media, *Drying Technol.*, *10*(4), 925–946, doi:10.1080/07373939208916488.
Or, D., P. Lehmann, E. Shahraeeni, and N. Shokri (2013), Advances in soil evaporation physics–A review, *Vadose Zone J.*, *12*(4), doi:10.2136/vzj2012.0163.
Persson, B. N. J., O. Albohr, U. Tartaglino, A. I. Volokitin, and E. Tosatti (2005), On the nature of surface roughness with application to contact mechanics, sealing, rubber friction and adhesion, *J. Phys. Condens. Matter*, *17*(1), R1–R62, doi:10.1088/0953-8984/17/1/R01.
Pillai, K. M., M. Prat, and M. Marcoux (2009), A study on slow evaporation of liquids in a dual-porosity porous medium using square network model, *Int. J. Heat Mass Transfer*, *52*(7–8), 1643–1656, doi:10.1016/j.ijheatmasstransfer.2008.10.007.
Prat, M. (1993), Percolation model of drying under isothermal conditions in porous media, *Int. J. Multiphase Flow*, *19*(4), 691–704, doi:10.1016/0301-9322(93)90096-D.
Prat, M. (2002), Recent advances in pore-scale models for drying of porous media, *Chem. Eng. J.*, *86*(5502), 153–164.
Prat, M. (2011), Pore network models of drying, contact angle, and film flows, *Chem. Eng. Technol.*, *34*(7), 1029–1038, doi:10.1002/ceat.201100056.
Rajaram, H., L. A. Ferrand, and M. A. Celia (1997), Prediction of relative permeabilities for unconsolidated soils using pore-scale network models, *Water Resour. Res.*, *33*(1), 43–52, doi:10.1029/96WR02841.
Shahraeeni, E., P. Lehmann, and D. Or (2012), Coupling of evaporative fluxes from drying porous surfaces with air boundary layer: Characteristics of evaporation from discrete pores, *Water Resour. Res.*, *48*, W09525, doi:10.1029/2012WR011857.
Shokri, N., P. Lehmann, and D. Or (2010), Liquid-phase continuity and solute concentration dynamics during evaporation from porous media: Pore-scale processes near vaporization surface, *Phys. Rev. E*, *81*(4), 046308, doi:10.1103/PhysRevE.81.046308.
Silvestrini, S., D. Ferraro, T. Tóth, M. Pierno, T. Carofiglio, G. Mistura, and M. Maggini (2012), Tailoring the wetting properties of thiolene microfluidic materials, *Lab Chip*, *12*(20), 4041–4043.
Suzuki, M., and S. Maeda (1968), On the mechanism of drying of granular beds, *J. Chem. Eng. Jpn.*, *1*(1), 26–31.
Toussaint, R., K. J. Måløy, Y. Méheust, G. Løvoll, M. Jankov, G. Schäfer, and J. Schmittbuhl (2012), Two-phase flow: Structure, upscaling, and consequences for macroscopic transport properties, *Vadose Zone J.*, *11*(3), doi:10.2136/vzj2011.0123.
Tsimpanogiannis, I. N., Y. C. Yortsos, S. Poulou, N. Kanellopoulos, and A. K. Stubos (1999), Scaling theory of drying in porous media, *Phys. Rev. E*, *59*(4), 4353–4365, doi:10.1103/PhysRevE.59. 4353.
United States Environmental Protection Agency (2016), *On-Line Tools for Site Assessment Calculation*. [Available online at https://www3.epa.gov/ceampubl/learn2model/part-two/onsite/estdiffusion-ext.html, last accessed 5 Apr 2017.]
Vorhauer, N., Y. J. Wang, A. Kharaghani, E. Tsotsas, and M. Prat (2015), Drying with formation of capillary rings in a model porous medium, *Transp. Porous Media*, *110*(2), 197–223, doi:10.1007/s11242-015-0538-1.
Xu, L., S. Davies, A. B. Schofield, and D. A. Weitz (2008), Dynamics of drying in 3D porous media, *Phys. Rev. Lett.*, *101*, 094502, doi:10.1103/PhysRevLett.101.094502.
Yiotis, A. G., I. N. Tsimpanogiannis, A. K. Stubos, and Y. C. Yortsos (2007), Coupling between external and internal mass transfer during drying of a porous medium, *Water Resour. Res.*, *43*, W06403, doi:10.1029/2006WR005558.
Yiotis, A. G., D. Salin, E. Tajer, and Y. C. Yortsos (2012), Drying in porous media with gravity-stabilized fronts: Experimental results, *Phys. Rev. E*, *86*(2), 026310, doi:10.1103/PhysRevE.86.026310.
Yiotis, A. G., D. Salin, and Y. C. Yortsos (2015), Pore network modeling of drying processes in macroporous materials: Effects of gravity, mass boundary layer and pore microstructure, *Transp. Porous Media*, *110*(2), 175–196, doi:10.1007/s11242-015-0529-2.